# Journal of Physics: Complexity

**PAPER**

# Next-day largest earthquake magnitude forecasting with the aid of Moon tidal force and sunspot data

Matheus Henrique Junqueira Saldanha[1,*] and Yoshito Hirata[2]

1 Degree Programs in Systems and Information Engineering, Graduate School of Science and Technology, University of Tsukuba, 1-1-1, Tennodai, Tsukuba, 305-8573 Ibaraki, Japan
2 Institute of Systems and Information Engineering, University of Tsukuba, 1-1-1, Tennodai, Tsukuba 305-8573, Ibaraki, Japan
* Author to whom any correspondence should be addressed.

**E-mail:** mhjsaldanha@gmail.com and hirata@cs.tsukuba.ac.jp

**Keywords:** earthquakes, Moon's gravity, solar activity, forced system

Supplementary material for this article is available online

## Abstract

Seismicity is a complex phenomenon with a multitude of components involved. In order to perform forecasting, which has yet to be done sufficiently well, it is paramount to be in possession of information of all these components, and use this information effectively in a prediction model. In the literature, the influence of the Sun and the Moon in seismic activity on Earth has been discussed numerous times. In this paper we contribute to such discussion, giving continuity to a previous work. Most importantly, we instrument four earthquake catalogs from different regions, calculating the Moon tidal force at the region and time of each earthquake, which allows us to analyze the relation between the tidal forces and the earthquake magnitudes. At first, we find that the dynamical system governing Moon motion is unidirectionally coupled with seismic activity, indicating that the position of the Moon drives, to some extent, the earthquake generating process. Furthermore, we present an analysis that demonstrates a clear positive correlation between tidal force and earthquake magnitude. Finally, it is shown that the use of Moon tidal force data and sunspot number data can be used to improve next-day maximum magnitude forecasting, with the highest accuracy being achieved when using both kinds of data. We hope that our results encourage researchers to include data from Moon tidal forces and Sun activity in their earthquake forecasting models.

## 1. Introduction

A glimpse into the literature shows that researchers have been investigating earthquake forecasting for decades already, but for most practical purposes we are still unable to forecast large events. Despite that, progress has been achieved in small steps in each subfield of earthquake forecasting. In this paper, we focus on next-day forecasting using, as main input data, earthquake catalogs that provide magnitude, location and depth of each earthquake. Such data is readily accessible for numerous regions around the world, so it is important to assess what the best forecasting accuracy is, which can be obtained with just such kind of data.

In the field, one method to contribute to earthquake forecasting is to identify and evaluate precursor phenomena. Many of them have been studied, including foreshocks and smaller fractures that supposedly precede larger events (Niemeijer *et al* 2010, Rivière *et al* 2018, Dorostkar and Carmeliet 2019), anomalous variations in Earth's electric and magnetic fields Draganov *et al* (1991), Fenoglio *et al* (1995), Fujiwara *et al* (2004), emissions of chemical gases from underground (Richon *et al* 2003, Ghosh *et al* 2009, Tareen *et al* 2019), and the list goes on.

Besides those, the effects of the Sun and the Moon and, more generally, of tidal forces on earthquakes, have been analyzed quite a few times in the literature (Ide *et al* 2016, Hao *et al* 2019). In Saldanha and Hirata (2022), we investigated the effects of the sunspot numbers, and gave evidence that it indeed influences earthquakes on Earth. Here, we focus on the tidal force exerted by the Moon, which is hypothesized to have

an influence on earthquakes because it is able to deform not only the ocean surface, but also the continental crust as well (Baker 1984, Volodichev *et al* 2003). Such movement could be a major player in the rate at which elastic strain energy builds up in faults, and also promote the appearance of cracks in the crust (nucleations) that can evolve into an earthquake.

## 2. Preliminaries

### 2.1. Datasets analyzed

The earthquake catalogs we used for analysis were obtained from: the GeoNet[3] project for New Zealand earthquakes, the Japanese Meteorological Agency[4] for earthquakes in Japan, the Department of Geophysics–Geothermics of the University of Athens[5] for earthquakes in the Balkan peninsula and surroundings, and the United States Geological Survey[6] for worldwide earthquakes. The period covered by the datasets was chosen to be from 1 January 2000 to 31 August 2021.

We have also used the sunspot data provided by the American Association of Variable Star Observers[7]. Besides that, the earthquake catalogs were instrumented with calculations of differential pulls exerted by the Moon using the invaluable tools provided by the Astropy library (Astropy Collaboration *et al* 2022).

### 2.2. Prediction framework

We use here the prediction framework proposed in Saldanha and Hirata (2022), of which we give a brief overview in the following. It consists mainly of calculating edit distances (Victor and Purpura 1997) between earthquake point patterns, and feeding these distances to a radial basis function network (Judd and Mees 1995).

Let $P_1 = \{t_1, \ldots, t_m\}$ and $P_2 = \{s_1, \ldots, s_n\}$ be two point patterns, then we can iteratively transform $P_1$ into $P_2$ using predetermined primitive operations. Each of these operations incurs a certain cost, and the edit distance is defined as the lowest possible cost necessary to do such transformation. The primitive operations and their associated costs are as follows:

**insertion** insert point $s_i$ into $P_1$, paying a cost of 1;
**deletion** remove point $t_i$ from $P_1$, paying a cost of 1; and
**shifting** replace point $t_i$ with $s_j$, paying a cost of $\lambda|s_j - t_i|$.

The hyperparameter $\lambda$ is meant to normalize the values $s_j$ and $t_i$ so that the particular time scale chosen (e.g. measured in seconds or in hours) does change the behavior of the algorithm. The above is easily extensible to the case where each point is accompanied by additional information (called **marks**), such as magnitude, depth etc. Consider the marked point patterns $P_1 = \{(t_1, \boldsymbol{u}_1), \ldots, (t_m, \boldsymbol{u}_m)\}$ and $P_2 = \{(s_1, \boldsymbol{v}_1), \ldots, (s_n, \boldsymbol{v}_n)\}$, with marks $\boldsymbol{u}_i, \boldsymbol{v}_j \in \mathbb{R}^d$. Then, the cost of insertion and deletion is maintained at 1, and the cost of shifting $(t_i, \boldsymbol{u}_i)$ onto $(s_j, \boldsymbol{v}_j)$ becomes (Schoenberg and Tranbarger 2008, Suzuki *et al* 2010, Hirata and Sukegawa 2019):

$$\text{cost} = \lambda_0 |t_i - s_j| + \sum_{k=1}^{d} \lambda_k |u_{i,k} - v_{j,k}|,$$

where $u_{i,k}$ denotes the $k$th coordinate of vector $\boldsymbol{u}_i$. Again, the hyperparameters $\lambda_k$ are supposed to normalize the values such that the costs are all comparable to each other.

For analyzing the catalogs, we prepared a time window of 7 days and slid it by 1 day along the time axis, collecting a set $\boldsymbol{x}_i$ of earthquake events for each window $i$; we note that the timestamp of an earthquake, after doing this process, is modified to be the time elapsed since the beginning of the time window it belongs to. This process was repeated for each catalog. The distances are fed to a radial basis function network, which finds a linear mapping with the form (Judd and Mees 1995):

$$\hat{z}(\boldsymbol{x}, \boldsymbol{w}) = w_0 + \sum_{i=1}^{k} w_i \, \psi \left( d_X(\boldsymbol{x}, \boldsymbol{c}_i) \right), \tag{1}$$

[3] www.geonet.org.nz/.
[4] www.data.jma.go.jp.
[5] www.geophysics.geol.uoa.gr/.
[6] https://earthquake.usgs.gov/earthquakes/search/.
[7] www.aavso.org/, data accessed through https://lasp.colorado.edu/lisird/.

**Figure 1.** Illustration of the data preparation and organization used in this project. The period considered was from 1st January 2000 up to 31st August 2021. Observed time windows have a length of 7 days, whereas forecast time windows are 1 day long. These windows are slid throughout the dataset on a per 1 day basis.
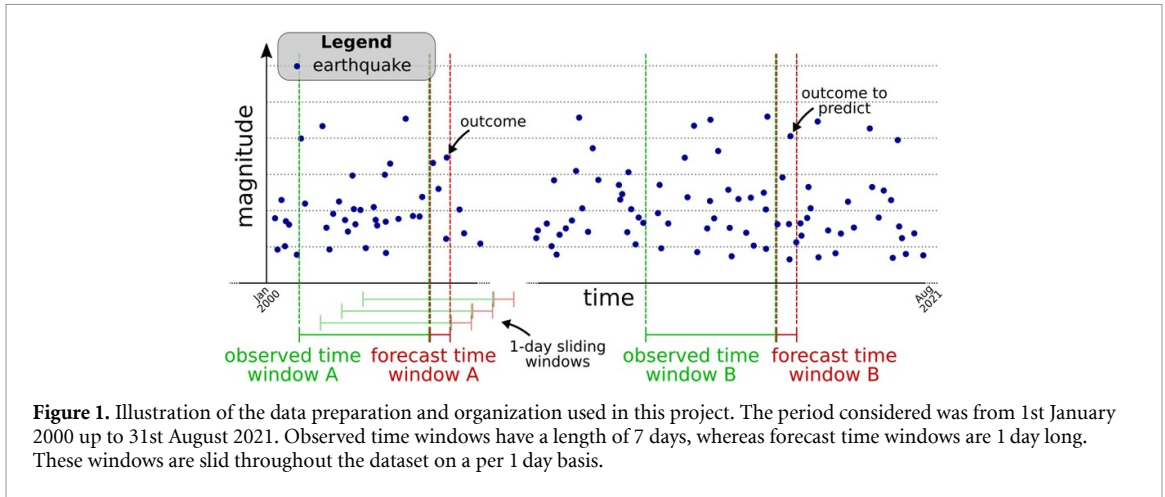
where $w$ are parameters found by least squares, and the equation is linear on the activation terms $\psi(d_X(x, c_i))$, with $d_X(x, c_i)$ being the edit distance between the earthquake point pattern of interest $x$ and a few selected instances from the training set $c_i$. In practice, the output $\hat{z}(x, w)$ is a prediction for either the maximum magnitude or total number of earthquakes above a certain threshold on the day following $x$.

Figure 1 further illustrates how the earthquake patterns are collected. There are two kinds of sliding time windows: observed time windows have a length of 7 days, whereas forecast time windows are 1 day long, and they are slid throughout the dataset on a 1 day by 1 day basis. We collect all earthquakes within a observed time window, but for the forecasting time window, we only take the largest earthquake magnitude. Listing 1 shows how this is done algorithmically.

Predictions are made by comparing an observed time window from the test set (observed time window B) to the observed time windows from the training set (such as observed time window A), using the edit distance as means of comparison. In the case of figure 1, if the distance between observed time windows A and B was very low, then we could predict the outcome of time window B as being the same outcome of time window A. In practice, we do not have just one observed time window, but rather, we select 100 observed time windows from the past, and take the weighted average of the respective outcomes. The weighing is automatically done by the radial basis function network (Judd and Mees 1995).

To include sunspot and Moon tidal force data into the above framework, we modify equation (1) as follows:

$$\hat{z}(x, y^{(1)}, y^{(2)}, w) = w_0 + \sum_{i=1}^{k} \left[ w_i \, \psi\left(d_X(x, c_i) + \kappa_1 d_E(y^{(1)}, y_{c_i}^{(1)}) + \kappa_2 d_E(y^{(2)}, y_{c_i}^{(2)})\right)\right], \qquad (2)$$

where $y^{(1)}$ is the vector containing the 7 sunspot numbers (one per day) referring to the same week that $x$ refers to, and $y_{c_i}^{(1)}$ is the same, but referring to the same week as $c_i$; the same reasoning applies to $y^{(2)}$ and $y_{c_i}^{(2)}$, but here these vectors refer to the 168-dimensional vector containing the hourly tidal force collected over the 7 day window (the force is calculated on an arbitrarily selected point around the center of the region). These vectors always have the same dimension, so we use the Euclidean distance $d_E$ here. Parameters $\kappa_1$ and $\kappa_2$ are normalizing constants to make the three kinds of distances to have values in the same order of magnitude on average.

In order to validate such prediction framework, we perform tests on toy models, which are presented in B.

## 2.3. Test for coupling between dynamical systems

In order to test the existence of a causality relationship between the Moon and earthquakes on Earth, we employ the methods proposed in (Andrzejak and Kreuz 2011) and (Hirata *et al* 2016), which work mainly upon the two distance matrices obtained by calculating the distances between embedded states after appropriately embedding the two time series (see appendix A for an overview of Dynamical Systems concepts and terms). In the case that one dynamical system drives the other, if distances for the forced system in the reconstructed space are near, then distances for the driving force are also near, while the opposite is not true; the methods of Andrzejak and Kreuz (2011) and Hirata *et al* (2016) test whether this relation exists in the two distance matrices provided to it. The idea is based on the embedding theorem for the forced system by Stark (Stark 1999).

**Listing 1.** Pseudocode illustrating the preparation of the earthquake point patterns that arise by collecting the earthquakes occurring in an observed time window and the respective forecast time window, as illustrated in figure 1. By the end of its execution, the *i*-th element of 'eqPointPatterns' represents an earthquake point pattern for a time window of 7 days, and the *i*-th element of 'maxMag' and 'logN' contains the maximum magnitude and the log amount of earthquakes on the day following such 7 day period.

```
 1 let 'catalog' <- the earthquake catalog
 2
 3 let 'eqPointPatterns' <- empty vector, will hold the earthquake point patterns
 4 let 'maxMag' <- empty vector, will hold the maximum magnitudes on each day
 5 let 'logN' <- empty vector, will hold the log amount of earthquakes on each day
 6
 7 # Observed time window size
 8 W = 7
 9
10 # Forecast time window size
11 PRED_W = 1
12
13 for eq in catalog:
14     let eq.dayNumber <- 1 + number of days elapsed from January 1st 2000 until
15                         the time of earthquake 'eq'
16
17 for i in W to (7913-PRED_W):
18     # 7913 is the total number of days covered by the catalog
19
20     let obsWindow <- { earthquakes from 'catalog' whose dayNumber
21                        lies within the interval [i---W + 1, i] }
22
23     let forecastWindow <- { earthquakes from 'catalog' whose dayNumber is (i + 1) }
24
25     eqPointPatterns.append( obsWindow )
26
27     maxMag.append("maximum magnitude observed in 'forecastWindow',
28                   or value 0 if 'forecastWindow' is empty")
29
30     let N <- "amount of earthquakes in 'forecastWindow'"
31     logN.append(log(N + 1))
```

Let us assume that $y_1^{(2)}, y_2^{(2)}, \ldots, y_n^{(2)}$ are the sequence of reconstructed states obtained by performing an embedding on the Moon tidal force time series, and that $x_1, x_2, \ldots, x_n$ are the reconstructed states that result from an embedding on the earthquake data. Now let $d_{\mathrm{E}}(y_i^{(2)}, y_j^{(2)})$ and $d_X(x_i, x_j)$ be appropriate metrics defined in these two reconstructed spaces, which in our case are the Euclidean metric as $d_{\mathrm{E}}$, and the edit distance as $d_X$. The method of Andrzejak and Kreuz (2011) operates on the two distance matrices resulting from these two metrics. Take the *i*th row in the distance matrix for $Y$ (the tidal force system), and find the smallest distance in that row, excluding the diagonal and $W$ elements adjacent to it (to avoid temporal correlation); assume that such element is the *j*th entry in the row, namely $d_{\mathrm{E}}(y_i^{(2)}, y_j^{(2)})$. Now take the element located at position $(i, j)$ in the distance matrix for $X$ (i.e. earthquakes), which is $d_X(x_i, x_j)$, and record its rank in that row after excluding the same diagonal elements as before. This element could be, for example, the fourth lowest distance in that row. By repeating this process for each row of the distance matrices, we obtain a collection of ranks $r_1, \ldots, r_n$, and if the system $Y$ does not drive $X$, these ranks are expected to be on average about half the number of non-excluded elements in a row, which for most rows is $(n - 2W)/2$ (recall that $W$ is a parameter to exclude the entries referring to states that might be close in space because they are close in time, and it is chosen depending on the parameters on the embedding performed to reconstruct the states $y_i^{(2)}$ and $x_j, \forall i, j \in \{1, \ldots, n\}$). Thus, for each row, call the number of non-excluded elements $K_i$ and let $G_i = (K_i + 1)/2$ be the expected rank if no coupling exists, then their method calculates the quantity (which can be called the 'A–K coupling index from $X$ to $Y$'):

$$L(Y \to X) = \frac{1}{n} \sum_{i=1}^{n} \frac{G_i - r_i}{G_i - 1}, \tag{3}$$

which is a number belonging to $[-1, 1]$, and the value 0 represents absence of coupling. It is straightforward to derive $L(X \to Y)$ using the same logic as above.

Hirata *et al* (2016) method works as follows. First, we normalize the distances such that the sets $\{d_\mathrm{E}(\boldsymbol{y}_i^{(2)}, \boldsymbol{y}_j^{(2)}) : 1 \leqslant i,j \leqslant n\}$ and $\{d_X(\boldsymbol{x}_i, \boldsymbol{x}_j) : 1 \leqslant i,j \leqslant n\}$ are constrained within $[0,1]$. We then take the set:

$$\left\{ \left( d_\mathrm{E}\left(\boldsymbol{y}_i^{(2)}, \boldsymbol{y}_j^{(2)}\right), d_X\left(\boldsymbol{x}_i, \boldsymbol{x}_j\right) \right) : 1 \leqslant i,j \leqslant n \right\},$$

these points will belong to $[0,1] \times [0,1]$. In case there is no coupling, then there should be no difference in the distribution of points if we take different slices of the region, such as $[0,1] \times [0, 0.25]$ and $[0,1] \times [0.25, 0.5]$ (or by slicing the left-hand interval and keeping the right-hand intact). On the other hand, if there existed a coupling from the Moon to earthquakes on Earth, then the points in $[0, 0.25] \times [0,1]$ would be in general nearer to the *x*-axis than in the other region slices, reflecting that small distances in the driving system tend to be associated with small distances in the driven system (which is the definition of dynamical coupling). In this context, the method of Hirata *et al* (2016) performs a statistical test for the presence of such behavior. In contrast to the example given above, however, the method considers that the $[0,1]$ interval is sliced into a user-defined number of bins. Of course, coupling on the opposite direction can be tested by merely inverting the meaning of values $\boldsymbol{y}_i^{(2)}$ for all *i*, and $\boldsymbol{x}_j$ for all *j*, above.

Like with the prediction framework, these coupling tests are also validated using toy models, as also presented in appendix B.

### 2.4. Tidal force calculation
As broadly known, the acceleration of the Earth towards the Moon is given by $a_\mathrm{M} = Gm_\mathrm{M}/d_\mathrm{M}^2$, where $m_\mathrm{M}$ is the mass of the Moon, $d_\mathrm{M}$ the distance between the Earth and Moon, and $G$ the gravitational constant. Bodies as huge as the Earth will have some portions nearer to the Moon (the 'ear side') and portions farther (the 'far side'), and due to the $d_\mathrm{M}^2$ term involved in the gravitational force, these two different portions of the Earth will be pulled towards the Moon with different intensities. Let $r_\mathrm{E} = 6.37 \times 10^6$ m be the approximate radius of the Earth, then an object with mass 1 located in the near side of the Earth is pulled towards the Moon with acceleration $a'_\mathrm{M} = Gm_\mathrm{M}/(d_\mathrm{M} - r_\mathrm{E})^2$, and most importantly, if we evaluate the difference $a'_\mathrm{M} - a_\mathrm{M}$, we get the relative acceleration of the object on the surface, when observed from the center of the Earth itself. The difference becomes:

$$a'_\mathrm{M} - a_\mathrm{M} = \frac{Gm_\mathrm{M}}{(d_\mathrm{M} - r_\mathrm{E})^2} - \frac{Gm_\mathrm{M}}{d_\mathrm{M}^2}$$

$$= Gm_\mathrm{M}\left[ \frac{1}{d_\mathrm{M}^2 - 2d_\mathrm{M}r_\mathrm{E} + r_\mathrm{E}^2} - \frac{1}{d_\mathrm{M}^2} \right]$$

$$= Gm_\mathrm{M}\left[ \frac{2d_\mathrm{M}r_\mathrm{E} - r_\mathrm{E}^2}{d_\mathrm{M}^4 - 2d_\mathrm{M}^3 r_\mathrm{E} + d_\mathrm{M}^2 r_\mathrm{E}^2} \right]$$

$$= Gm_\mathrm{M}\frac{d_\mathrm{M}}{d_\mathrm{M}^4}\left[ \frac{2r_\mathrm{E} - r_\mathrm{E}^2/d_\mathrm{M}}{1 - 2r_\mathrm{E}/d_\mathrm{M} + r_\mathrm{E}^2/d_\mathrm{M}^2} \right]$$

now since $d_\mathrm{M} \gg r_\mathrm{E}$, we can eliminate the terms $r_\mathrm{E}/d_\mathrm{M}$, and also because $2r_\mathrm{E} \gg r_\mathrm{E}^2/d_\mathrm{M}$, the right-hand term can be also removed from the numerator, thus yielding the approximation (Sawicki 1999):

$$a'_\mathrm{M} - a_\mathrm{M} \approx Gm_\mathrm{M}\frac{d_\mathrm{M}}{d_\mathrm{M}^4}\frac{2r_\mathrm{E}}{1}$$

$$= \frac{2Gm_\mathrm{M}r_\mathrm{E}}{d_\mathrm{M}^3}, \tag{4}$$

commonly called 'differential pull.' An object in the near-side surface of the Earth would move towards the Moon with this acceleration, if the Earth did not exert any gravitational force on that object. One implication of this is that objects on the surface of the Earth are slightly lighter (if measured using a scale) than we would expect from the well known formula $m \cdot g$.

Interestingly, the exact same effect occurs in the far-side of the Earth surface, and with the same magnitude of differential pull. The point here is that the Earth is pulled towards the Moon with more intensity than the object in the far side of the surface, so if the Earth gravity did not exist, the object on the surface would be 'left behind' with a speed equivalent to the differential pull found above. The calculations for this are very similar to the above, but for the difference:

$$a_\mathrm{M} - a''_\mathrm{M} = \frac{Gm_\mathrm{M}}{d_\mathrm{M}^2} - \frac{Gm_\mathrm{M}}{(d_\mathrm{M} + r_\mathrm{E})^2}.$$

The above equations were used to calculate the differential pulls at each region and at each hour. We calculated the position of Earth and Moon using Astropy, which, when making calculations for periods of time in the past, offers values with more than sufficient accuracy for our purposes here. By doing this, we are also implicitly dealing with the variable sidereal period of the Moon, which can vary ∼3.5 h about the average value (estimated using Astropy, also see Wilkinson (2010)). In this sense, our method differs, for example, from what is done in Hao *et al* (2019), whose conclusions concerning Moon influences are mainly based on approximating its period as being fixed.

We note that we are aware of the existence of models for mathematical models for the calculation of differential pulls and other physical quantities associated to tidal forces (Longman 1959, Agnew 2005). However, since Astropy gives us very accurate positions of the Earth, Sun and Moon when considering time points in the past, we consider that using such data would be better than using mathematical models that cannot capture all the gravitational interactions (including those resulting from other planets in our Solar System) concerning each of these three bodies. Of course, using mathematical models allows performing analyses farther in the future. However, in our prediction model, we only need to know the heavenly body positions up to the present date and time, which would already allow us to make a prediction for next 7 days. If for any reason the actual positions are not available or cannot be obtained algorithmically, we note that Astropy is also very accurate for estimating the trajectory of the Earth, Sun and Moon in the near future (Astropy Collaboration *et al* 2022).

## 3. Results

The influence of the Moon on earthquakes has been analyzed various times in the literature. However, while those studies tend to focus more on finding correlations between those two phenomena, we opt for another approach, one that detects causality instead; in this sense, we note that correlation does not necessarily imply causality (Liang 2014). Having determined the existence of causality, we also investigate whether the strength of tidal forces can be used to improve accuracy of earthquake forecasting.

By using the method of Andrzejak and Kreuz (2011), as explained in section 2.3, we found that the Moon drives earthquakes (represented by $Y \to X$, with $Y$ being Moon effects) to some extent, since $L(Y \to X)$ is usually much larger (in absolute value) than $L(X \to Y)$; the one exception is the Touhoku case, where a negative value was observed for $L(Y \to X)$, but this kind of situation is difficult to interpret, and can probably be attributed to the large changes in earthquake frequency and magnitudes in Touhoku around the year of 2011 (see table 1). Besides that, unidirectional coupling is also identified when we use the method of Hirata *et al* (2016), since the *p*-values for the $Y \to X$ case are in general a lot smaller than for $X \to Y$ (table 1), except for the Japan case, where such relation is inverted, and in fact it indicates that earthquakes drive Sun electromagnetic activity, but surely there must have been stochastic factors that led this case to behave differently from the others. We see that in most cases (but not all), the methods indicate a coupling $Y \to X$, so it can be concluded, from table 1, that there is evidence to believe that such a coupling indeed exists.

Besides dynamical coupling, we also analyzed the direct relation between the differential pull and the magnitude of each earthquake. Here, although the emphasis is in correlation (rather than causation (Liang 2014)), the results below should still serve to strengthen the analysis presented above. Figure 2 shows what happens if we take the average differential pulls of all earthquakes with magnitude greater than or equal to a threshold *m*, which is represented by the *x*-axis. The lines stop as soon as the number of earthquakes above that threshold is lower than 25, otherwise we would observe a sudden increase in the instability of the lines as the threshold increases. What we observe here is a clear tendency of the average differential pull to increase as the magnitude threshold increases, which thus indicates a tendency of larger magnitude earthquakes to happen when there is a higher tide.

However, note that, when compared to the maximum differential pull encountered in the instrumented datasets, most cases display only a moderate increase (ranging between 9.3% and 31.1%) relative to the average differential pull in the corresponding dataset. In other words, although the tendency seems to exist, it is very far from meaning that earthquakes tend to occur when the moon is at nadir or zenith, for example; what is most meaningful here is that the Moon tidal force seems to be positively correlated with the earthquake magnitudes.

That said, it might be worth remarking that analyzing correlation directly with the two time series (magnitude and differential pulls) in the dataset is made difficult since the number of earthquakes with lower magnitudes is a lot larger than those with larger magnitudes. We also remark that, in figure 2, the upper bound on the magnitude threshold for the worldwide dataset ended up being lower than for the Japanese one, even though the latter is supposed to be a subset of the former. This is because the datasets come from different sources, and the calculation of the magnitude differs between them, giving some differences in the magnitude assigned to the same earthquake (an average difference of 0.3, but that can reach up to 1.6).

**Table 1.** Results of applying the coupling tests of Andrzejak and Kreuz (2011) (represented by the A–K coupling indices $L(Y \rightarrow X)$ and $L(X \rightarrow Y)$) and Hirata *et al* (2016) (represented by the $p$-values) on the datasets considered in this paper. Here $Y$ corresponds to Moon tidal effects, whereas $X$ represents earthquakes.

| | Japan | Touhoku | New Zealand | Balkan | West Balkan |
|---|---|---|---|---|---|
| $L(Y \rightarrow X)$ | 0.015 | $-0.018$ | 0.043 | 0.058 | 0.035 |
| $L(X \rightarrow Y)$ | $-0.008$ | 0.002 | $-0.002$ | $-0.003$ | $-0.015$ |
| $p$-value $Y \rightarrow X$ | 0.072 | 0.041 | $9.06 \times 10^{-4}$ | $5.29 \times 10^{-6}$ | $1.47 \times 10^{-5}$ |
| $p$-value $X \rightarrow Y$ | $4.83 \times 10^{-6}$ | 0.140 | $3.70 \times 10^{-3}$ | 0.012 | 0.043 |
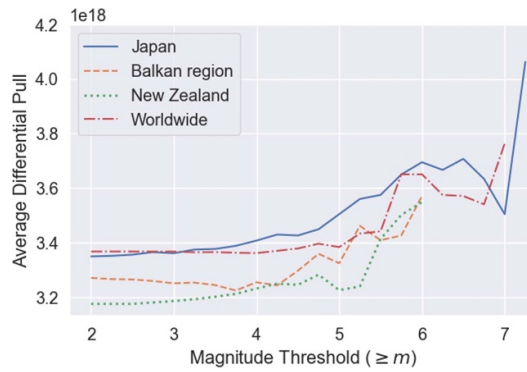


**Figure 2.** Average differential pull of the earthquakes above the threshold given in the $x$-axis. The lines stop when there are less than 25 earthquakes in the calculation of the average. We observed an increase for every earthquake catalog analyzed.

**Table 2.** Hypothesis tests comparing the differential pulls of the 20% smallest earthquakes against those of the earthquakes whose magnitudes are above the thresholds 5, 5.25, 5.5, 5.75 and 6 (as indicated in the first row of the table). The values in the table display the $p$-values obtained with a Wilcoxon rank-sum test. Values in boldface represent a rejected null hypothesis at a significance level of 5%.
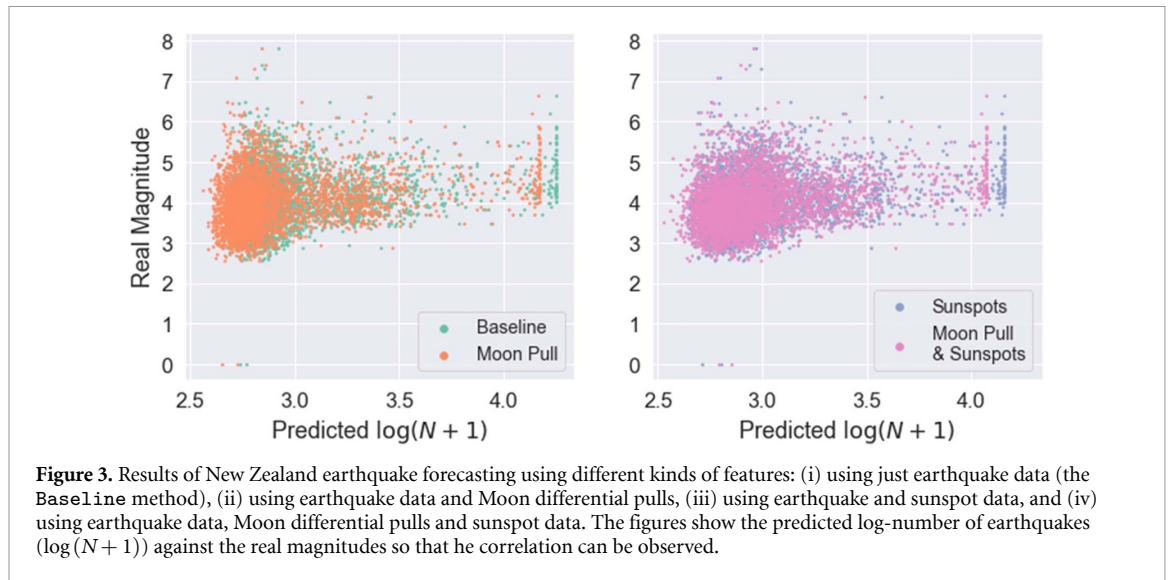
| | Magnitude threshold | | | | |
|---|---|---|---|---|---|
| Region | $>5$ | $>5.25$ | $>5.5$ | $>5.75$ | $>6$ |
| Japan | $\mathbf{3 \times 10^{-8}}$ | $\mathbf{1 \times 10^{-8}}$ | $\mathbf{1 \times 10^{-7}}$ | $\mathbf{1 \times 10^{-7}}$ | $\mathbf{5 \times 10^{-7}}$ |
| New Zealand | 0.18 | 0.27 | **0.03** | **0.05** | 0.07 |
| Balkan | 0.13 | **0.01** | $\mathbf{4 \times 10^{-3}}$ | **0.03** | **0.01** |

Table 2 shows a direct comparison between smallest magnitude earthquakes with higher magnitude ones. Here, we compare the 20% smallest with the earthquakes above each threshold shown in the second row of the table, and then perform a Wilcoxon rank-sum test to compare the median differential pulls of both sets of earthquakes. The alternative hypothesis here is 'the earthquakes with larger magnitudes have larger differential pulls.' In the table, we see the null hypothesis is rejected in more than two thirds of the cases, at a significance level of 5%. Thus, again, indicating that a larger differential pull tends to be associated with earthquakes with larger magnitude.

We then proceeded to try verifying how data from the Sun and the Moon can affect forecasting accuracy. The forecasting algorithm used here is as delineated in section 2.2, and we remark that the choice of the parameters $\kappa_1$ and $\kappa_2$ was as follows. After performing an embedding in each of the three kinds of data (earthquakes, sunspots and moon differential pulls), we end up with reconstructed states, denoted respectively by the indexed sequences $\boldsymbol{x}_i$, $\boldsymbol{y}_j^{(1)}$ and $\boldsymbol{y}_k^{(2)}$, which are separated in training and test sets. For each kind of data, we calculate the pairwise distances within the training set, resulting in three symmetric distance matrices $D_X$, $D_Y^{(1)}$ and $D_Y^{(2)}$. Let $m(D)$ represent the average of the lower triangle part of matrix $D$, then $\kappa_1$ and $\kappa_2$ are chosen so that:

$$\kappa_1 \cdot m\left(D_Y^{(1)}\right) = \frac{m(D_X)}{2} \quad \text{and}$$
$$\kappa_2 \cdot m\left(D_Y^{(2)}\right) = \frac{m(D_X)}{2},$$

where we take half the mean of the distances in the earthquake dynamical system so that it is not overwhelmed by the other two distances in equation (2).

**Figure 3.** Results of New Zealand earthquake forecasting using different kinds of features: (i) using just earthquake data (the `Baseline` method), (ii) using earthquake data and Moon differential pulls, (iii) using earthquake and sunspot data, and (iv) using earthquake data, Moon differential pulls and sunspot data. The figures show the predicted log-number of earthquakes ($\log(N+1)$) against the real magnitudes so that he correlation can be observed.

The prediction results are shown in figures 3–8. Besides the correlation, we also calculate the odds-ratio (another metric of accuracy) by performing a binary forecasting, where we associate the event 'the maximum magnitude on a day will be larger than a fixed threshold $\alpha$' to the event 'the predicted log number of earthquakes on that day is larger than a constant $\beta$'. This results in a confusion matrix:

|  | max. magnitude $> \alpha$ | max. magnitude $\leqslant \alpha$ |
|---|---|---|
| $\log(N+1) > \beta$ | A | B |
| $\log(N+1) \leqslant \beta$ | C | D |

where $A, B, C$ and $D$ are the number of cases that fulfill the conditions shown in the respective row and column. The odds-ratio is then given by $A \cdot D / B \cdot C$, providing insights into the odds of correct positive predictions compared to incorrect ones. Higher odds ratios indicate a more favorable balance between true positives and false positives, suggesting better predictive performance. The odds-ratio was collected for each trial, and they are shown in the boxplots in figures 4–8.

In figure 3 we show an example of predictions made for the New Zealand case, where we predict the logarithm of the number of earthquakes ($\log(N+1)$, with $N$ being the number of earthquakes), and correlate it to the actual magnitude of these earthquakes (both these quantities are related by the Gutenberg–Richter's law (Stein and Wysession 2003, Saldanha and Hirata 2022)); we do not predict the maximum magnitudes directly because they are less regular than the log-number of earthquakes, and this approach demonstrated better results. For earthquakes in Japan (figure 4), an improvement in correlation is observed when using data from the Moon tides, and an even larger increase (5.37% improvement) when both Moon tidal force data and sunspot data are used. However, when using sunspot data only, the improvement is negligible. Here, odds-ratio was not improved by using Moon tidal force data or sunspot data individually, but there is a 3.51% increase when using both sunspot and Moon tidal force data.

Figure 5 shows results for the Touhoku region, which is a subset of the Japan data. In this case, the average correlation obtained is considerably larger than for the Japan nationwide case; in fact, we have observed that analyzing smaller regions tend to lead to the better accuracy, a phenomenon that we will be further analyzing in future work. The accuracy gain brought by including sunspot data and Moon tidal force data is also more noticeable, with up to a 29.62% increase when using both Moon tidal force data and sunspot data; however, similarly to the Japan case, using sunspot data alone leads to a lower improvement (in odds-ratio as well). When including all three kinds of data, we get a 76.63% increase in odds-ratio, which is also remarkable.

For New Zealand (figure 6), we see that in this case sunspot data was more relevant in terms of correlation, with a 8.86% increase. Including Moon tidal force data on top of sunspot data actually led to a smaller improvement in the correlation; the odds-ratio, however, increased 5.72%, which is more than when using sunspot data and Moon tidal force data individually.

Finally, figures 7 and 8 show results for the Balkan region and a subregion located in its west side, where there is a large concentration of earthquakes. Again, by restricting the analysis to a subregion, we ended up obtaining far larger average correlations. In both cases, substantial increases in correlation and odds-ratio are attained when including sunspot data or Moon tidal force data, and the highest values are seen when using all three kinds of data simultaneously.
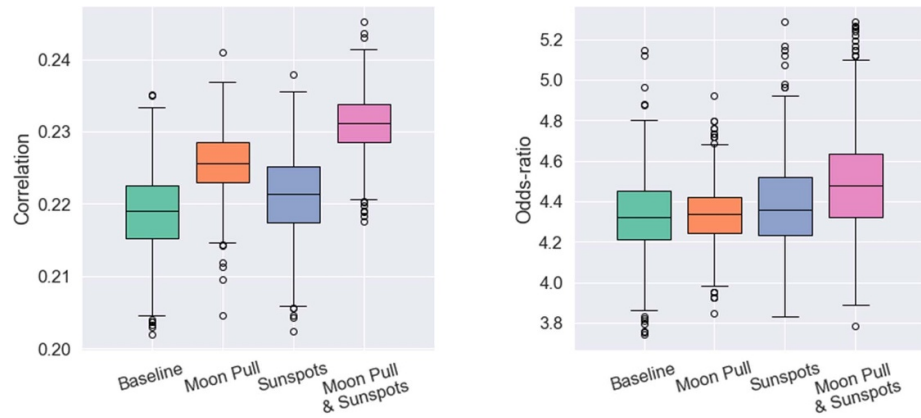
**Figure 4.** Correlation and odds-ratios for predicting earthquakes in Japan nationwide, using different settings of data sources. In the `Baseline` model, only earthquake data is used, and in the other settings we use: (i) earthquake and Moon data, (ii) earthquake and sunspot data, and (iii) earthquake, Moon and sunspot data. The thresholds for calculating the odds-ratio were chosen as $\alpha = 6$ (for the real magnitudes) and $\beta = 3.2$ (for the predicted values). The improvements in correlation median (relative to the `Baseline`) were: 2.90%, 0.82%, 5.37%, respectively. In odds-ratio median, they were: 0%, 0.77%, 3.51%.
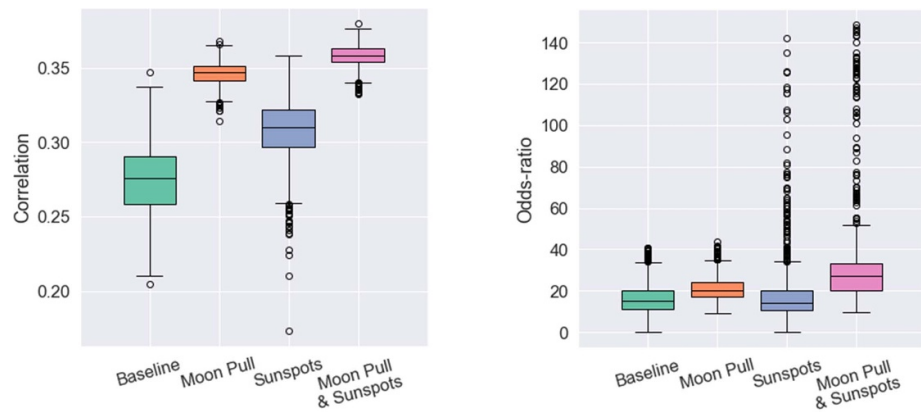


**Figure 5.** Correlation and odds-ratios for predicting earthquakes in the Touhoku region of Japan. Thresholds $\alpha = 4.5$ and $\beta = 3$ for calculating the odds-ratio. Improvements in correlation median: 25.32%, 11.72%, 29.62%, respectively. In odds-ratio median: 37.37%, 1.36%, 76.63%. See caption of figure 4 for further details.
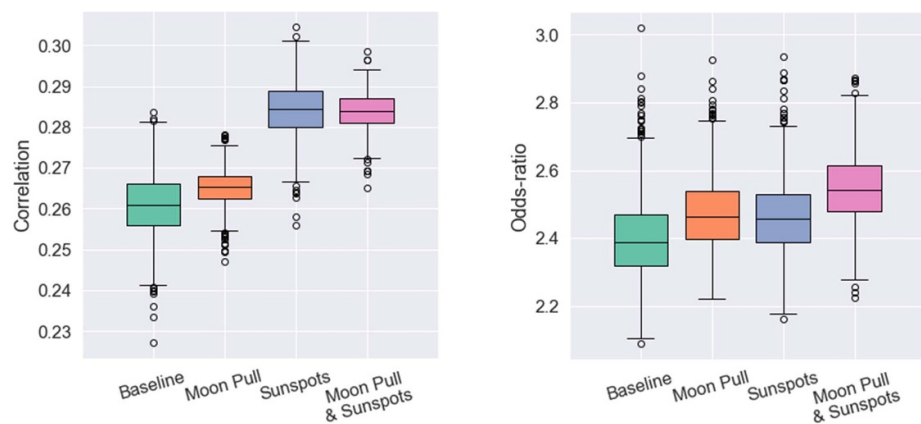


**Figure 6.** Correlation and odds-ratios for predicting earthquakes in New Zealand. Thresholds $\alpha = 4.25$ and $\beta = 3.25$ for calculating the odds-ratio. Improvements in correlation median: 1.59%, 8.86%, 8.77%, respectively. In odds-ratio median: 2.92%, 2.91%, 5.72%. See caption of figure 4 for further details.
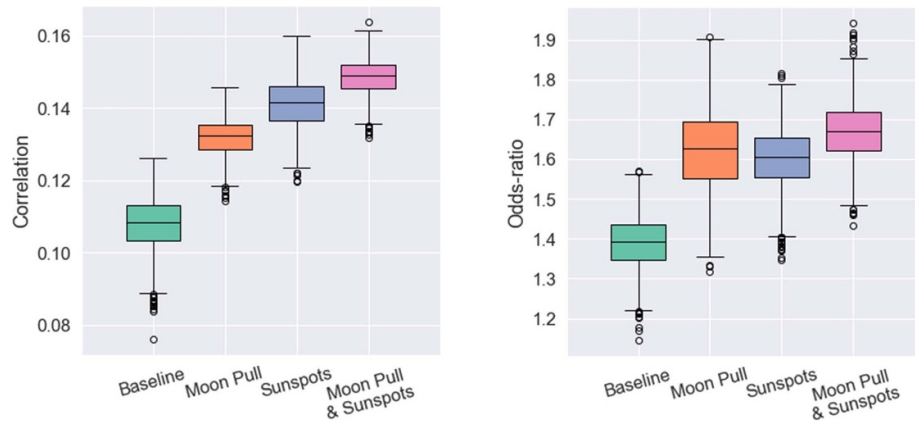
**Figure 7.** Correlation and odds-ratios for predicting earthquakes around the Aegean plate. Thresholds $\alpha = 4$ and $\beta = 3.5$ for calculating the odds-ratio. Improvements in correlation median: 22.59%, 31.25%, 38.02%, respectively. In odds-ratio median: 16.51%, 15.03%, 20.62%. See caption of figure 4 for further details.
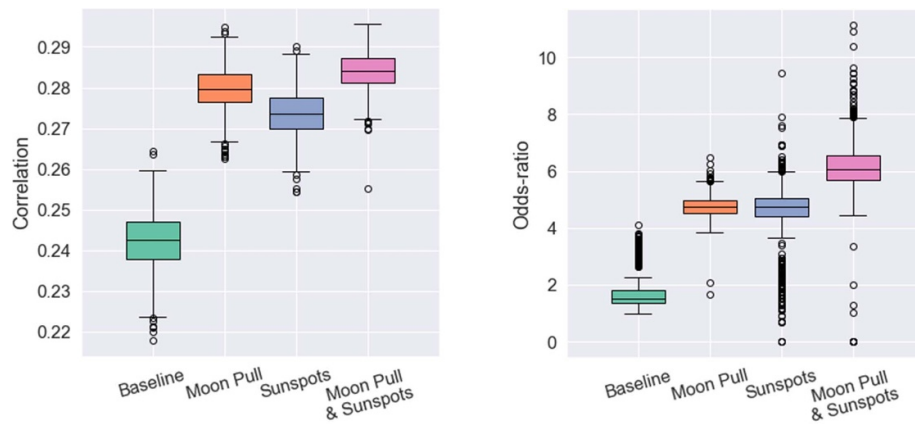


**Figure 8.** Correlation and odds-ratios for predicting earthquakes in a western region of the Aegean plate. Thresholds $\alpha = 4$ and $\beta = 3.25$ for calculating the odds-ratio. Improvements in correlation median: 15.24%, 12.83%, 17.13%, respectively. In odds-ratio median: 213.29%, 211.39%, 300.03%. See caption of figure 4 for further details.

## 4. Conclusion

In this paper, we have presented evidence that support existing hypotheses that earthquakes are affected by entities external to the Earth, namely, the Sun and the Moon. We had begun to analyze the case of sunspot numbers in previous work (Saldanha and Hirata 2022), but here it has been extended to demonstrate that the conclusions also apply very well to the Balkan peninsula region (and its west subregion), thus strengthening our previous results.

As for the Moon, we found that the coupling detection tools from dynamical systems indicate that the motion of the Moon is unidirectionally coupled with the generating process of earthquakes, meaning that the position of the Moon has an influence on the latter, although the extent of this influence cannot be inferred from these methods alone. Subsequently, we used planetary motion simulation to calculate the Moon differential pull at the region of each earthquake in the moment they occurred, and analyzed the relation of these forces with the magnitude of earthquakes. To the best of our knowledge, although there are related work discussing the correlation between the amount of earthquakes and the Moon tidal forces (Métivier *et al* 2009) as well as the correlation between the magnitudes of earthquakes and the combined effects of the Sun-Moon tidal forces (Ide *et al* 2016), the combined 'causal' effects of sunspot numbers and the Moon tidal force on earthquakes on the Earth had not been investigated yet. Our analysis strongly indicates the existence of causal relation between the Moon tidal force and the magnitude of earthquakes, which we interpreted as a slight-to-moderate tendency of larger earthquakes to occur when the tidal force is relatively large at the position they occur. Finally, we showed that next-day magnitude forecasting accuracy can be improved by using Moon tidal force data, and improved even more by using *both* Moon tide and sunspot information.

We hope that our results encourage the use of Moon tide and sunspot information to improve earthquake forecasts, so future work should endeavor to design forecasting algorithms that can use these heterogeneous kinds of data more effectively. We also highlight that our work is limited in the sense that only next-day maximum magnitudes are forecast, with no regard whatsoever to where the earthquake will occur. A difficulty arises here since the representation of the spatial dimension in terms of latitude and longitude appear to be inadequate for forecasting the position of earthquakes; further exploration of this problem is left as future work.

## Data availability statement

All data that support the findings of this study are included within the article (and any supplementary files).

## Acknowledgments

## Appendix A. Overview of dynamical systems terms and concepts

A dynamical system is characterized by a set of states $S \subset \mathbb{R}^n$ and a function $F$ that describes their evolution in time, such that given some state $s_t$ in time $t$, we can predict the state at time $s_{t+\Delta t}$ as $s_{t+\Delta t} = F(s_t, \Delta t)$. $F$ can be defined for every positive $\Delta t$, as is common if the system arises from a system of differential equations, or just for $\Delta t \in \mathbb{N}$, in cases where the system is observed in discrete time intervals. Given an initial state $s_0$, the evolution over time of this state defines a trajectory $\{F(s_0, \Delta t) : \Delta t \in \mathbb{R}$ or other appropriate infinite sets$\}$, and for many systems, this trajectory converges to a set $\mathcal{A}$ for a vast number of possible choices of $s_0$. In fact, $\mathcal{A}$ is called an attractor if the set of choices of $s_0$ has non-zero measure.

We rarely, if ever, observe the states $s_t$ directly. Rather, we observe consequences of the system, such as mass, temperatures etc. This is represented by an observation function $\varphi$ and a time series $\{\varphi(s_{t_i}) : i \in \mathbb{N}\}$ that results from observing the system at times $t_1, t_2, \ldots$. If we measure the temperature of mixture of chemical reagents over time, then that is our $\varphi$. The exact form of $\varphi$ does not matter, only its output does. The revolutionary idea of Dynamical Systems is that, given just these measurements, we can have a very good idea of what the underlying attractor looks like, which gives us information about the trajectory of the underlying states and, as a consequence, allows us to predict the respective measurements (given by $\varphi$) that will be observed in future points in time.

The main concept that allows this is that of an 'embedding.' An embedding is an injective function from a compact set (such as an attractor) into $\mathbb{R}^m$. It might seem problematic to ensure that the chosen function is injective (i.e. ensure that the function will not cause self-intersections $f(a) = f(b)$) after it is applied over the compact set. However, a theorem by Whitney ([1936](#)) states that if a compact set $A$ is a $d$-dimensional manifold, 'most' functions $f : A \to \mathbb{R}^m$ with $m > 2d$ will be an embedding. This only applies to 'generic' functions, which is a huge class; functions that are not generic are exceptions. Takens ([1981](#)) used this result to prove that $f$ can be substituted by the function that returns a vector of delayed measurements:

$$h(t) = \left( \varphi(s_t), \varphi(s_{t-d}), \varphi(s_{t-2d}), \ldots, \varphi(s_{t-(m-1)d}) \right)$$

where $\varphi(s_t)$ is the measurement of the system taken at time $t$. This works only when the measurements form a uniformly sampled time series (as is the case of our sunspot and lunar tides data).

This is called Takens' embedding, or delay coordinates embedding, and the resulting high-dimensional vectors are called reconstructed states or embedded states. This provides a way to bring experimental measures into a high-dimensional space in a way that points corresponding to different states do not overlap. This is not always helpful, as points can still be too close from each other to be algorithmically distinguished, which is further made complicated by stochastic data influences.

## Appendix B. Tests on toy models

In order to demonstrate the applicability of the prediction framework described in section 2.2, we perform here two tests on toy models. We assume that the relation of earthquakes and the Moon is comparable to a periodically forced dynamical system. Additionally, since earthquakes are non-uniformly sampled time series caused by a sudden release of strain energy that builds up continuously, we take the set of local maxima of the corresponding chaotic time series to simulate such situation.

The first two toy models make use of the periodically forced Rössler system (taken from Betancourt-Mar *et al* (2005)):

$$\begin{cases} x' = -(y+z) \\ y' = x + ay + d\sin\dfrac{2\pi}{T} \\ z' = b + z(x-c) \end{cases}$$

where $a$, $d$, $T$ and $c$ are parameters of the model. The driving force here is the term $d\sin\frac{2\pi}{T}$. We take one of the set of parameters mentioned in (Betancourt-Mar *et al* 2005): $a = 0.1$, $b = 0.1$, $c = 9$, $d = 10$ and $T = 6.066$. We then simulate this model with initial condition $(x_0, y_0, z_0) = [0.1, 0.1, 0.1]$.

The other two toy models use the periodically forced Lorenz system described in (Sun *et al* 2012):

$$\begin{cases} x' = 10(y-x) \\ y' = (24 - 4c_0\sin(u))x - xz + c_0\sin(u)y \\ z' = xy - 8z/3 \\ u' = \omega \end{cases}$$

where $c_0$ and $\omega$ are the parameters of the model, and we take $c_0 = 1$ and $\omega = 7$, chosen from figure 2 in (Sun *et al* 2012) so that the system is chaotic. The driving force here is the term $c_0\sin(u)$. The same initial condition $(x_0, y_0, z_0) = [0.1, 0.1, 0.1]$ is used.

We integrate the Rössler system numerically from $t_0 = 0$ to $t_F = 30\,000$ in steps of $\Delta t = 0.01$, generating 3 million points, of which the first 500 thousand are discarded. We take the set of local maxima of the resulting time series on the $x$ axis.

With this, we begin by applying the same prediction framework described in section 2.2 to the non-uniformly sampled time series of local maxima, as well as the uniformly sampled time series of the driving force $d\sin(2\pi/T)$. We use time windows of length $k \cdot 7$ to predict the maximum value on the subsequent time window of length $k \cdot 1$, where $k = 4$ ($k = 2$ for the Lorenz system) proved to yield time windows with a minimally sufficient number of events in each time window so that prediction could be performed. Similar to what we did in the text, we also collect the values of the driving force within the time window of length $k \cdot 7$, sampling it every 1 units of time (yielding 28 samples).

Then we calculate the edit distances for the sets of local maxima, and also the Euclidean distances between the corresponding 28-dimensional vectors of values taken from the driving force, which yields two distance matrices that we can then feed to the RBF algorithm. Again, the distance matrices are normalized so that their means are approximately equal, and the $\lambda_k$ of the edit distance algorithm is taken in the exact same way as we did for earthquakes, including the random selection of 100 instances from the training set to feed the radial basis functions.

Figure B1 shows the results of the predictions, clearly demonstrating that by including information about the driving force, we manage to increase the prediction accuracy.

The procedure that the Lorenz system underwent is very similar, and we highlight the differences in the following. $t_F$ is taken to be $10\,000$ instead, which generates 1 million points, whose 50 thousand first points are discarded; and the driving force for the Lorenz system can be seen as the sine function $\sin(u)$, where $u$ is a variable that does not exist in the usual Lorenz equations. We emphasize that, similar to the Rössler case, the local maxima are also taken from the resulting time series on the $x$ axis. Figure B2 shows the results, and the same conclusion can be drawn here as with figure B1.

Also using the same system of equations, we also perform predictions performing a delay-coordinate embedding directly on the time series of local maxima. In particular, we used a embedding with dimension $m = 6$ and delay $d = 1$, giving rise to a series of vectors $\boldsymbol{v}_1, \ldots, \boldsymbol{v}_n$ for the forced system, and the vectors for the driving force were obtained by collecting the value of the driving force ($d\sin(2\pi/T)$) at the same point in time as the values in the vectors $\boldsymbol{v}_1, \ldots, \boldsymbol{v}_n$. In other words, we generated a new series of vectors $\boldsymbol{u}_1, \ldots, \boldsymbol{u}_n$ where $\boldsymbol{u}_i$ is the value of the driving force at the time where each value $v \in \boldsymbol{v}_i$ occurred.
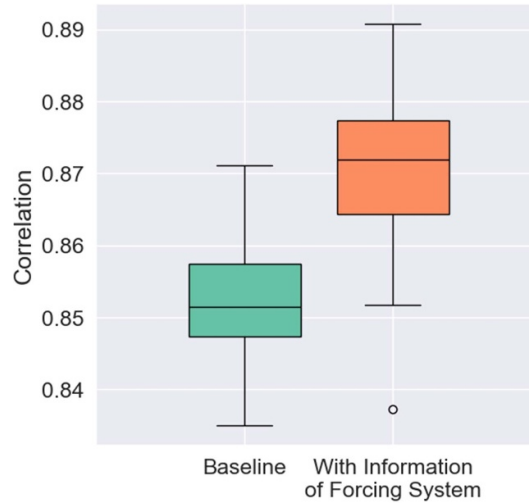
**Figure B1.** Results of applying the prediction framework described in section 2.2 to a toy model concerning a numerically simulated periodically forced Rössler system of differential equations. The local maxima is taken along the *x* axis of the system, so as to mimic the earthquake behavior.
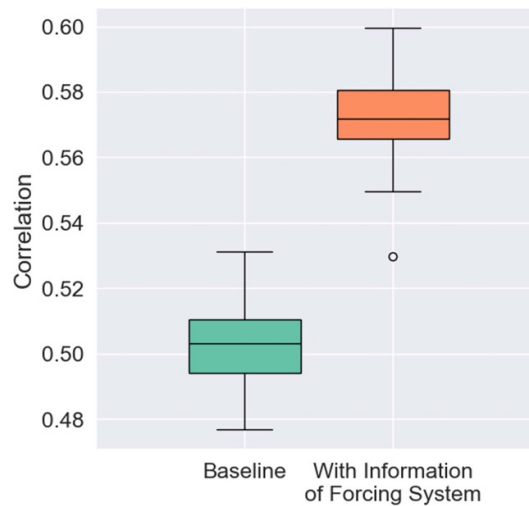


**Figure B2.** Results of applying the prediction framework described in section 2.2 to a toy model concerning a numerically simulated periodically forced Lorenz system of differential equations. The local maxima is taken along the *x* axis of the system, so as to mimic the earthquake behavior.

Then we calculate the pairwise Euclidean distances among the vectors $v_1, \ldots, v_n$, and also the pairwise Euclidean distances among the vectors $u_1, \ldots, u_n$, which yields two distance matrices that we use in the same as we used for earthquakes. The prediction results are as shown in figure B3, where the inclusion of the complete information about both systems increases the correlation slightly and also reduces the variance of prediction significantly.

For the Lorenz system, once again $t_F$ is taken to be 10 000 instead, and the first 50 thousand simulated points are discarded. The rest of the procedure was executed in the exact same manner, and the results can be found in figure B4, where we again observe a higher correlation and lower variance therein.

We have also applied the coupling test of Andrzejak and Kreuz (2011) to all the toy models. Let $X$ represent the forced system and $Y$ the driving force, then for the Rössler model using time windows, we had $(L(Y \to X), L(X \to Y)) = (0.005, -0.001)$, and using delay coordinates these values were $(0.006, -0.002)$. For the Lorenz model using time windows we obtained $(0.010, -0.004)$, and using delay coordinates it was $(0.003, -0.006)$.

Thus, for all cases, the values of $L(Y \to X)$ have the correct sign and are statistically significant at a significance level of 0.1, except for the Lorenz model using delay coordinates. The values of $L(X \to Y)$ are all negative, which does not have any particular meaning.
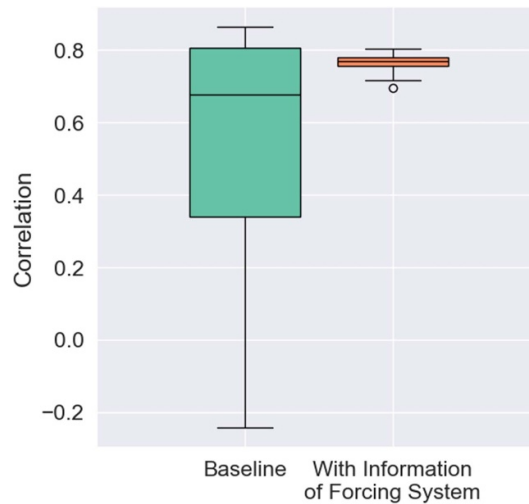
**Figure B3.** Results of applying the prediction framework described in section 2.2 to a toy model concerning a numerically simulated periodically forced Rössler system of differential equations. The local maxima is taken along the $x$ axis of the system, so as to mimic the earthquake behavior.
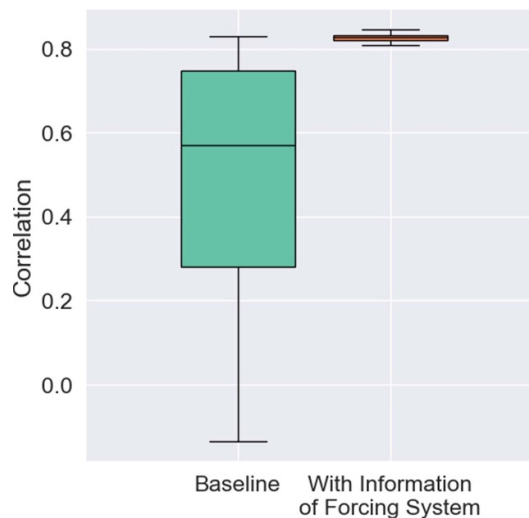


**Figure B4.** Results of applying the prediction framework described in section 2.2 to a toy model concerning a numerically simulated periodically forced Lorenz system of differential equations. The local maxima is taken along the $x$ axis of the system, so as to mimic the earthquake behavior.

Initially, we expected the coupling results to be more prominent, since it is a toy model running in perfect conditions, but we conjecture that since the systems are forced by a simple sine function and at a quite modest coupling strength, the simplicity of such driving force makes it more difficult to detect the coupling. In fact, if we substitute the driving force in the Rössler model by the time series generated by another Rössler model, we observe $L(Y \to X) = 0.025$, which is sensibly higher than the ones observed above.

## ORCID iDs

Matheus Henrique Junqueira Saldanha ⬤ https://orcid.org/0000-0001-7701-5583
Yoshito Hirata ⬤ https://orcid.org/0000-0002-9245-2543

## References

Agnew D C 2005 *Earth Tides: An Introduction* (University of California)
Andrzejak R G and Kreuz T 2011 Characterizing unidirectional couplings between point processes and flows *Europhys. Lett.* **96** 50012
Baker T 1984 Tidal deformations of the earth *Sci. Prog.* **69** 197–233
Betancourt-Mar J A, Alarcón-Montelongo I S and Nieto-Villar J M 2005 The Rössler system as a model for chronotherapy *J. Phys.: Conf. Ser.* **23** 58

Dorostkar O and Carmeliet J 2019 Grain friction controls characteristics of seismic cycle in faults with granular gouge *J. Geophys. Res.: Solid Earth* **124** 6475–89

Draganov A, Inan U and Taranenko Y N 1991 ULF magnetic signatures at the earth surface due to ground water flow: a possible precursor to earthquakes *Geophys. Res. Lett.* **18** 1127–30

Fenoglio M A, Johnston M J and Byerlee J D 1995 Magnetic and electric fields associated with changes in high pore pressure in fault zones: application to the Loma Prieta ULF emissions *J. Geophys. Res.: Solid Earth* **100** 12951–8

Fujiwara H, Kamogawa M, Ikeda M, Liu J, Sakata H, Chen Y, Ofuruton H, Muramatsu S, Chuo Y and Ohtsuki Y 2004 Atmospheric anomalies observed during earthquake occurrences *Geophys. Res. Lett.* **31** L17110

Ghosh D, Deb A and Sengupta R 2009 Anomalous radon emission as precursor of earthquake *J. Appl. Geophys.* **69** 67–81

Hao J, Zhang J and Yao Z 2019 Evidence for diurnal periodicity of earthquakes from midnight to daybreak *Natl Sci. Rev.* **6** 1016–23

Hirata Y, Amigó J M, Matsuzaka Y, Yokota R, Mushiake H, Aihara K and Ma J 2016 Detecting causality by combined use of multiple methods: climate and brain examples *PLoS One* **11** e0158572

Hirata Y and Sukegawa N 2019 Two efficient calculations of edit distance between marked point processes *Chaos* **29** 101107

Ide S, Yabe S and Tanaka Y 2016 Earthquake potential revealed by tidal influence on earthquake size-frequency statistics *Nat. Geosci.* **9** 834–7

Judd K and Mees A 1995 On selecting models for nonlinear time series *Physica* D **82** 426–44

Liang X S 2014 Unraveling the cause-effect relation between time series *Phys. Rev. E* **90** 052150

Longman I 1959 Formulas for computing the tidal accelerations due to the Moon and the Sun *J. Geophys. Res.* **64** 2351–5

Métivier L, de Viron O, Conrad C P, Renault S, Diament M and Patau G 2009 Evidence of earthquake triggering by the solid earth tides *Earth Planet. Sci. Lett.* **278** 370–5

Niemeijer A, Marone C and Elsworth D 2010 Frictional strength and strain weakening in simulated fault gouge: competition between geometrical weakening and chemical strengthening *J. Geophys. Res.: Solid Earth* **115** B10207

Richon P, Sabroux J-C, Halbwachs M, Vandemeulebrouck J, Poussielgue N, Tabbagh J and Punongbayan R 2003 Radon anomaly in the soil of Taal volcano, the Philippines: a likely precursor of the M 7.1 Mindoro earthquake (1994) *Geophys. Res. Lett.* **30** 1481

Rivière J, Lv Z, Johnson P and Marone C 2018 Evolution of b-value during the seismic cycle: insights from laboratory experiments on simulated faults *Earth Planet. Sci. Lett.* **482** 407–13

Saldanha M H J and Hirata Y 2022 Solar activity facilitates daily forecasts of large earthquakes *Chaos* **32** 061107

Sawicki M 1999 Myths about gravity and tides *Phys. Teach.* **37** 438–41

Schoenberg F P and Tranbarger K E 2008 Description of earthquake aftershock sequences using prototype point patterns *Environmetrics* **19** 271–86

Stark J 1999 Delay embeddings for forced systems. I. Deterministic forcing *J. Nonlinear Sci.* **9** 255–332

Stein S and Wysession M 2003 *An Introduction to Seismology, Earthquakes and Earth Structure* (Wiley-Blackwell)

Sun K, Liu X, Zhu C and Sprott J 2012 Hyperchaos and hyperchaos control of the sinusoidally forced simplified Lorenz system *Nonlinear Dyn.* **69** 1383–91

Suzuki S, Hirata Y and Aihara K 2010 Definition of distance for marked point process data and its application to recurrence plot-based analysis of exchange tick data of foreign currencies *Int. J. Bifurcation Chaos* **20** 3699–708

Takens F 1981 Detecting strange attractors in turbulence *Dynamical Systems and Turbulence, Warwick 1980* ed D Rand and L-S Young (Springer) pp 366–81

Tareen A D K, Asim K M, Kearfott K J, Rafique M, Nadeem M S A, Iqbal T and Rahman S U 2019 Automated anomalous behaviour detection in soil radon gas prior to earthquakes using computational intelligence techniques *J. Environ. Radioact.* **203** 48–54

The Astropy Collaboration *et al* 2022 The Astropy project: sustaining and growing a community-oriented open-source project and the latest major release (v5.0) of the core package *Astrophys. J.* **935** 167

Victor J D and Purpura K P 1997 Metric-space analysis of spike trains: theory, algorithms and application *Netw., Comput. Neural Syst.* **8** 127–64

Volodichev N, Kuzhevskij B, Nechaev O Y, Panasyuk M, Podorol'sky A and Shavrin P 2003 Solar-lunar-terrestrial interactions: bursts of neutron emission and seismic activity *Int. J. Geomagn. Aeron.* **4** 251–4

Whitney H 1936 Differentiable manifolds *Ann. Math.* **37** 645

Wilkinson J 2010 *The Moon in Close-up: A Next Generation Astronomer's Guide* (Springer Science & Business Media)